Theor Chem Acc (2009) 124:179–186
DOI 10.1007/s00214-009-0596-y

REGULAR ARTICLE

DFT studies of pressure effects on structural and vibrational properties of crystalline octahydro-1,3,5,7-tetranitro-1,3,5,7-tetrazocine

Weihua Zhu · Xiaowen Zhang · Tao Wei · Heming Xiao

Received: 5 March 2009 / Accepted: 3 June 2009 / Published online: 18 June 2009

Abstract A detailed study of the structural, electronic, and vibrational properties of crystalline octahydro-1,3,5,7-tetranitro-1,3,5,7-tetrazocine (HMX) under hydrostatic pressure of 0–100 GPa was performed with density functional theory (DFT). The results show that the compressibility of HMX crystal is anisotropic. With the increasing pressure, the lattice constants and cell volumes calculated by local density approximation (LDA) gradually approach these by the PW91 functional of generalized gradient approximation (GGA). The band gap reduction is more pronounced in the low-pressure range compared to the high-pressure region. The band gaps calculated by LDA and GGA pseudopotential plane-wave reproduce the trend of pressure-induced variation of band gap by all electron calculations. The calculated pressure-induced frequency shifts indicate that the pressure produces a more significant influence on the ring deformation and stretching vibrations than on other modes. The vibrational modes associated with the motions of the CH_2 and NO_2 side groups are quite sensitive to pressure. The mixing between different vibrational modes becomes stronger under compression. Our results also show that DFT can well describe the intermolecular interactions in HMX under high pressure.

Keywords Density functional theory · HMX · Hydrostatic pressure · Band gap · Vibrational properties

W. Zhu (✉) · X. Zhang · T. Wei · H. Xiao (✉)
Institute for Computation in Molecular and Materials Science and Department of Chemistry, Nanjing University of Science and Technology, 210094 Nanjing, China
e-mail: zhuwh@mail.njust.edu.cn

H. Xiao
e-mail: xiao@mail.njust.edu.cn

1 Introduction

Octahydro-1,3,5,7-tetranitro-1,3,5,7-tetrazocine (HMX) is one of the most widely used energetic ingredient in various high-performance explosives and propellant formulations due to its thermal stability and high detonation velocity relative to other explosives [1, 2]. Over the past several decades a large number of studies have been devoted to the structural properties and decomposition mechanism of HMX. Unfortunately, many fundamental and practical problems of HMX are still not well understood because it possesses a complex chemical behavior. Thus, HMX continues to inspire new research efforts [3–21] to better understand its structure and thermal decomposition.

HMX experiences enormous pressure effects during the detonation process. Therefore, one fundamental aspect of its decomposition and burning is its structure during a high-pressure explosion. Although the detailed decomposition mechanism by which HMX releases energy under mechanical shock is still not well understood, it has been suggested that its decomposition may result from transferring thermal and mechanical energy into the internal degrees of freedom of tightly bonded groups of atoms in solid [22–24]. In addition, interpreting and understanding shock-induced chemical decomposition of energetic material requires the knowledge of the mechanical response of the material. Therefore, the knowledge of the structural and vibrational properties of HMX under high pressure appears to be very important in understanding its decomposition and burning.

The investigation of the microscopic properties of energetic materials remains to be a challenging task. An important challenge for experimental measurements is to study the pressure effects in energetic materials. Many experiments were carried out to investigate the structure

and decomposition of HMX under different pressures [3, 12, 23–26] and shock loading [14, 27, 28]. However, despite these efforts, little work has been done to investigate the structure and vibrational properties of HMX with the increasing pressure. In fact, a few studies on HMX under high pressure report many discrepancies. These discrepancies indicate the complexity and incomplete understanding of the structural properties of HMX. An alternative approach is atomistic simulation, an effective way to model the physical and chemical properties of complex solids at the atomic level as a complement to experimental work. Recently, density functional theory (DFT) method with pseudopotentials and a plane-wave basis set has been well-established and has been successfully applied to study the structures and properties of energetic solids under hydrostatic compression effect [18, 29–40]. There have been many theoretical studies on compression of crystalline β-HMX. Zerilli and Kuklja [17] have used Hartree-Fock approximation method to investigate the structural properties of crystalline 1,1-diamino-2,2-dinitro-ethylene and β-HMX under hydrostatic compression of 0–11 GPa. Byrd and Rice [18] have studied the crystal structures of five energetic molecular crystals including HMX over the pressure range of 0–10 GPa by using the three DFT functionals. Later, Lian et al. [20] have employed DFT method to examine the structural properties of β-HMX under hydrostatic compression up to 40 GPa. Recently, Conroy et al. [21] have performed DFT calculations to investigate the structures of β-HMX under hydrostatic and uniaxial compression. These studies are centered on the structural properties of β-HMX under compression up to low pressure. Little work has been done to investigate their vibrational properties with the increasing pressure.

In this study, we performed periodic DFT calculations to study the structural, electronic, and vibrational properties of HMX under hydrostatic pressure of 0–100 GPa. The atomic positions and the unit-cell parameters were allowed to relax to the minimum energy configuration to investigate the crystal structure at different pressures. Next we examined the variations in electronic structure under compression. Finally we discussed the pressure effects on the vibrational properties.

The remainder of this paper is organized as follows. A brief description of our computational method is given in Sect. 2, results and discussion are given in Sect. 3, and a summary of our conclusions is given in Sect. 4.

2 Computational method

The calculations performed in this study were done using the DFT method with Vanderbilt-type ultrasoft pseudopotentials [41] and a plane-wave expansion of the wave functions as implemented in the CASTEP code [42]. The self-consistent ground state of the system was determined by using a band-by-band conjugate gradient technique to minimize the total energy of the system with respect to the plane-wave coefficients. The electronic wave functions were obtained by a density-mixing scheme [43] and the structures were relaxed by using the Broyden, Fletcher, Goldfarb, and Shannon (BFGS) method [44]. The local density approximation (LDA) functional proposed by Ceperley and Alder [45] and parameterized by Perdew and Zunder [46] named CA–PZ, was employed. The cutoff energy of plane waves was set to 300.0 eV. Brillouin zone sampling was performed by using the Monkhost–Pack scheme with a k-point grid of $4 \times 3 \times 3$. Table 1 presents experimental and relaxed lattice constants at different cutoff energy of plane waves for crystalline HMX. The results show that the cutoff energy of 300.0 eV may be a compromise between computation efficiency and accuracy. The computational parameters adopted here were demonstrated to be reasonable by our previous study [19].

To compare with experiments, we used the crystal structure of β-HMX at ambient pressure and temperature as input structure. The experimental crystal structure of β-HMX [47] was first relaxed to allow the ionic configurations, cell shape, and volume to change at ambient pressure. Then from this relaxed structure, we applied hydrostatic compression of 0–100 GPa. All the calculations are based on the same crystal structure of HMX. In the geometry relaxation, the total energy of the system was converged $<2.0 \times 10^{-5}$ eV, the residual force <0.05 eV/Å, the displacement of atoms <0.002 Å, and the residual bulk stress <0.1 GPa. Based on the equilibrium, the phonon frequencies at the gamma point have been calculated from the response to small atomic displacements using linear response theory [48].

3 Results and discussion

3.1 Crystal structures

The LDA and PW91 (the generalized gradient approximation (GGA) proposed by Perdew and Wang [49])

Table 1 Experimental and relaxed lattice constants (Å) at different cutoff energy of plane waves with a k-point grid of $4 \times 3 \times 3$ for crystalline HMX

	Expt [47]	Cutoff energy (eV)				
		300	400	500	600	700
a	6.540	6.539	6.385	6.375	6.379	6.374
b	11.050	11.030	10.321	10.310	10.309	10.302
c	8.700	8.689	8.498	8.500	8.504	8.488
β	124.3°	123.9°	124.5°	124.6°	124.6°	124.5°

functionals were used to fully relax bulk HMX without any constraint at different pressures. The effect of pressure on the lattice constants of HMX is shown in Fig. 1. The results show that our calculated variation trend of the lattice constants with the increasing pressure is reproduced by the experiments [3, 14]. The LDA and PW91 results present similar variation trend: the lattice constants gradually decrease with the increasing pressure. In the whole pressure range, the lattice constants calculated by PW91 are larger than those by LDA. Previous studies [18] on cyclotrimethylenetrinitramine (RDX), 1,3,5-triamino-2,4,6,-trinitrobenzene (TATB), and pentaerythritol tetranitrate (PETN) under compression have shown that GGA generally overestimates lattice constants, while LDA underestimates the lattice constants when compared to experiments. This is consistent with our results here.

It is seen from Fig. 1 that the *b* axis is the most compressible, whereas the *c* axis essentially remains unchanged with pressure, which are in agreement with the experimental reports [3, 14]. The largest compression of the unit cell takes place in the pressure region of 0–30 GPa. With the increasing pressure from about 30 GP, the lattice parameters decrease slowly and the lattice constant *a* parallels *c*. The lattice constant *c* versus pressure curve crosses the *b* versus pressure one at about 30 GPa. The structure is much stiffer in the *a* and *c* direction than along the *b* axis. This shows that the compressibility of HMX crystal is anisotropic. Figure 2 displays the variation of the unit-cell angles with the increasing pressure. The non-continuous behavior in Fig. 2 may be due to numerical fluctuations. The results show that our calculations are in reasonable agreement with previous measurements [3, 14]. In the pressure range from 0 to 50 GPa, the deviation of the unit-cell angle β remains very small, while β increases slightly after that. Throughout the overall pressure range the unit-cell angles α and γ remain unchanged.

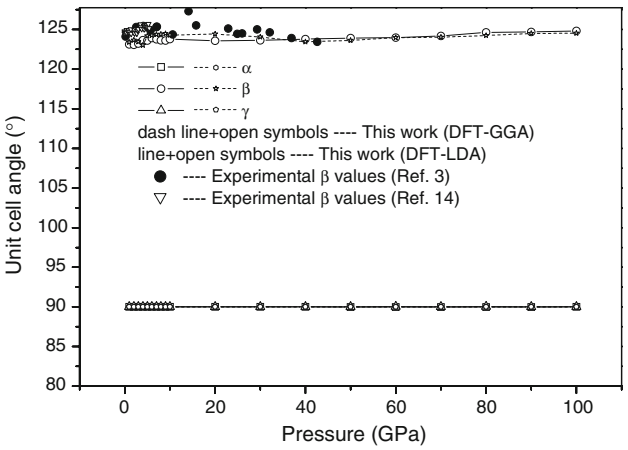

Fig. 2 Unit-cell angles of HMX as a function of hydrostatic pressure

Pressure-induced changes of the unit-cell volumes are presented in Fig. 3 together with available experimental data. Our calculated results well reproduce the trend of pressure-induced variation of volume by the experiments [3, 14]. At a given pressure, the experimental unit-cell volume is underestimated by our LDA calculations but overestimated by our GGA-PW91 results. This is consistent with previous DFT studies on several energetic solids [18]. As the pressure increases, the volume decreases monotonically. Up to 80 GPa the volume compression is 52%. The dependence of the LDA volume on pressure was determined by fitting the calculated values to the Murnaghan equation [50]. When the fit is done in the pressure range of 0–30 GPa we obtain a bulk modulus of 13.07 GPa, which is close to the experimental values of 12.4 GPa [3] and 13.5 GPa [25] but smaller than the theoretical value of 14.53 GPa based on empirical MD [4].

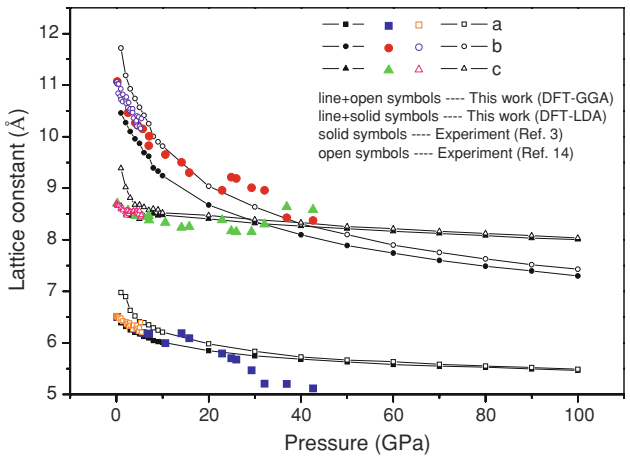

Fig. 1 Lattice constants of HMX as a function of hydrostatic pressure

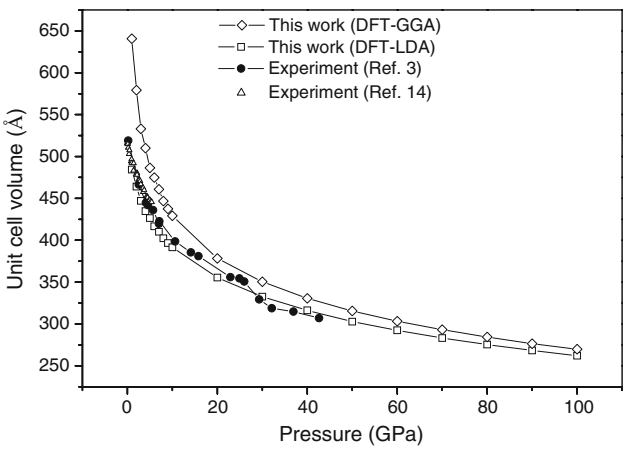

Fig. 3 Unit-cell volumes of HMX as a function of hydrostatic pressure

It is seen from Fig. 3 that as the pressure increases, our calculated results gradually approach the experimental values; moreover, the cell volumes calculated by LDA are close to these by GGA-PW91. This shows that the DFT calculations performed under high pressure might be more reliable due to the enhanced intermolecular interaction. It is well-know that conventional formulations of DFT do not include dispersion interactions and appears to be inadequate for studies of organic molecular crystals weakly bonded by van der Waals forces at low pressures. However, there is evidence that DFT can better treat weakly bound molecular systems under sufficient degrees of compression [18, 31]. Our calculations also show that DFT can well describe the intermolecular interactions in HMX crystal under high pressure. Also, note that the errors in the LDA results are slightly smaller than that in the GGA results in comparison with the experimental values. The LDA functional was used in the following calculations.

3.2 Electronic structures

Figure 4 displays the effect of pressure on the band gap of HMX. As the pressure increases, the band gap gradually decreases without any significant discontinuity. This is because the decrease of intermolecular space under compression leads to an increase of the overlap of different groups of bands and hence to the increase of charge overlap and delocalization in the system. However, in different pressure ranges, the average decrease of the band gap is different. When applying a linear fit in the different pressure ranges, the average decrease of the band gap up to 5 GPa is 0.066 eV/GPa, 0.024 eV/GPa from 5 to 10 GPa, and 0.008 eV/GPa from 10 to 100 GPa. This shows that the energy reduction is more pronounced in the low-pressure range compared to the high-pressure region, which is in agreement with previous theoretical studies on anthracene [51] and nitromethane [31] under high pressure. With a compression of 52% ($p = 80$ GPa), the band gap drops from 3.62 eV at ambient pressure [19] to 2.07 eV. In the pressure region of 0–20 GPa, the decrease of band gap is 1.05 eV. This magnitude is higher than the pressure-induced band gap reduction of 0.23 eV in nitromethane [31] from DFT calculations up to 20 GPa and of about 0.63 eV in anthracene [51] using DFT–LDA method up to 10 GPa. It is seen from Fig. 4 that there is no significant change of the band gap in the vicinity of the pressure 39 GPa, which is close to the detonation pressure of HMX determined by experiment [52]. This shows that compressing the crystal HMX to a pressure, an order of magnitude higher than that observed in developed detonation waves, is not sufficiently low to provide a significant thermal population of conduction electrons at detonation temperatures. Previous theoretical studies on nitromethane [29, 31], RDX [53], and lead azide [54] have shown that these materials also indicate some band gap lowering under compression to densities associated detonation, but not enough to produce a significant population of excited states at detonation temperatures. These observations agree qualitatively with our results here.

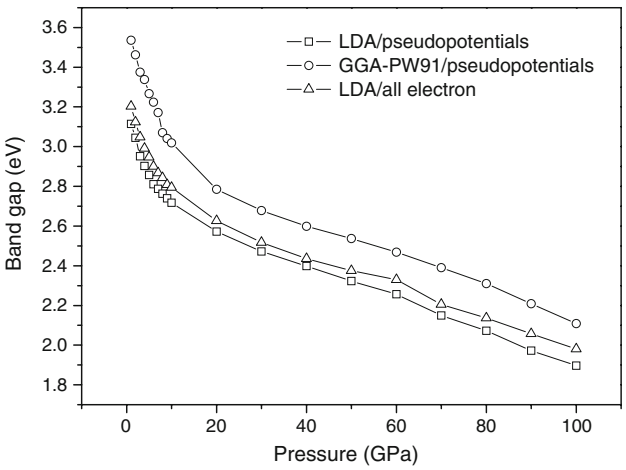

Fig. 4 Band gaps of HMX as a function of hydrostatic pressure

The band gaps by the GGA-PW91 and all electron calculations are also listed for comparison. The all electron calculations were performed with the DMol3 program package [55, 56] employing the LDA functional [57] and a double numerical basis functions augmented by polarization functions (DNP) [55]. The results show that the band gaps by pseudopotential calculations reproduce the trend of pressure-induced variation of band gap by all electron calculations. It can be inferred from Fig. 4 that there is a band gap closure in the system and HMX has metallic properties. Gilman [58] has proposed metallization at the shock front resulting from bending of covalent bonds. Such metallization has been also found to occur under hydrostatic compression in the covalently bonded energetic materials nitromethane [29] and RDX [53].

Finally, we try to correlate the HMX's stabilities (or explosive characters) under compression with the electronic structure. Previous theoretical studies [59, 60] have shown the relationship between the band gap and impact sensitivity for the metal azides. Our recent reports on the heavy-metal azides [61], the nitro anilines [62], the K-doped cuprous azides [63], the four HMX [19], and CL-20 [33] polymorphs within the framework of periodic DFT have also confirmed the relationship between the band gap and impact sensitivity. Gilman [64–67] has emphasized the role of HOMO–LUMO (highest occupied molecular orbital–lowest unoccupied molecular orbital) gap closure in the explosion of molecules suffering shear strain. Further investigations [68, 69] on the excitonic mechanism of detonation initiation show that the pressure

inside the impact wave front reduces the band gap between valence and conducting bands and promotes the HOMO–LUMO transition within a molecule. These studies have suggested that the HOMO–LUMO gap in gas molecules suffering shear strain, impact wave, or distortion can be directly related to the sensitivity. It can be thus expected that the smaller the band gap is, the easier the electron transfers from valence band to conduction band, and the more HMX becomes decomposed and exploded. A possible explanation may be that the increased sensitivity is caused by the increased number of excited states due to pressure-induced optical band gap reduction [70]. As can be seen in Fig. 4, the band gap of HMX gradually decreases with the increment of pressure. Our further calculations (not presented here) show that a band gap closure is at about 320 GPa. Therefore, it may be inferred that the impact sensitivity for HMX becomes more and more sensitive with the increasing pressure. This is supported by numerous experimental observations that an applied pressure increases the sensitivity of explosives to detonation initiation [71].

3.3 Vibrational properties

In this section, we turn to investigate the vibrational frequencies of HMX under compression. Both the internal modes due to intramolecular interactions and the lattice modes due to intermolecular interactions were considered here. Figure 5 displays the frequency shifts of representative lattice vibrations in the region of 30–80 cm^{-1} and of NO_2 twisting modes in the region of 80–120 cm^{-1} for HMX. As the pressure increases, all of these modes shift toward higher vibrational frequencies (so-called mode hardening). However, in different pressure ranges, the average increase of the frequency is different. The

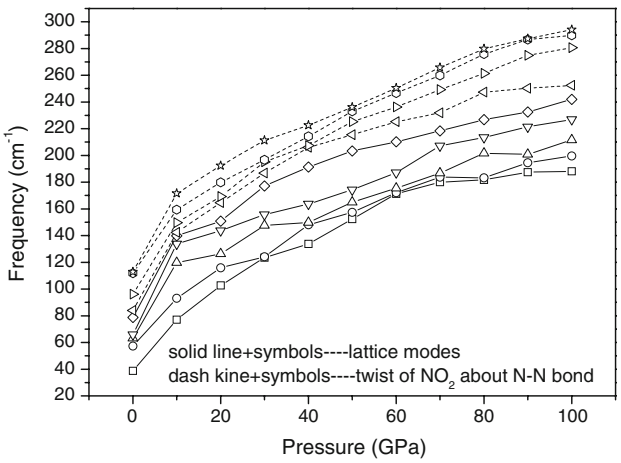

Fig. 5 Pressure-induced frequency shifts of lattice modes and NO_2 twisting modes for HMX

fluctuation behavior for the lattice modes in Fig. 5 is caused by numerical errors. This shows that DFT method cannot well describe extremely low energy lattice modes. The results agree with recent theoretical studies on RDX under compression [37]. Note that compression can also enhance the mixing between the NO_2 twisting and lattice modes. Table 2 presents a comparison of the linear fitted coefficients for the pressure-induced frequency shifts in the different pressure ranges. It is found that the frequency increase is more pronounced in the low-pressure range compared to the high-pressure region, and furthermore, different vibrational modes show distinctly different pressure-dependent behaviors. The coefficients for pressure-induced frequency shifts of the NO_2 twisting are larger than those of the lattice modes. This shows that the hydrostatic compression produces a more significant influence on the intramolecular interactions than on the intermolecular interactions.

The pressure-induced frequency shifts of ring deformation modes for HMX are displayed in Fig. 6a. The ring deformation modes are collective vibrations of all of the CN bonds on the ring. All of these modes shift toward higher vibrational frequencies under compression. As with the modes in the low-frequency range, the average increase of the frequency is different in different pressure ranges. It can be seen from Table 2 that the frequency increase is more pronounced in the low-pressure range compared to the high-pressure region; moreover, different vibrational modes show different pressure-dependent behaviors. Also, it is found that the frequency shifts of the ring deformation modes are the largest ones among all the modes. The ring deformation is related to important initial decomposition reaction, the concerted symmetric ring fission that produces four $CH_2N_2O_2$ molecules [72]. Therefore, the ring scission reaction of HMX would be favorable under high pressure. Figure 6b displays the pressure dependence of the vibrational frequencies of ring stretching and N–N stretching modes. To validate the reliability of our results, we also compare our calculated pressure-induced shifts of the vibrational frequencies for HMX with available experimental values [3] in Fig. 6b. Qualitatively, our calculations are in reasonable agreement with the experimental values. However, the errors between the calculated and experimental results under low pressure are larger than those under high pressure. This shows that the DFT calculations performed under high pressure might be more reliable than under low pressure due to the enhanced intermolecular interaction. It is obvious that different vibrational modes show clearly different pressure-dependent behaviors. The mode M5 associated with N–N stretching exhibits a pronounced shift and the fitted coefficient is 2.62 cm^{-1}/GPa. The ring stretching mode M2 and mode M3 also display a significant shift with the coefficients of 2.33 and

Table 2 Coefficients (cm^{-1}/GPa) for the pressure-induced shift of vibrational frequencies of HMX from the linear fit of our calculated results in two pressure ranges

Frequency range (cm^{-1}) at 0 GPa	Assignment	0–50 GPa	0–100 GPa
30–80	Lattice vibration	1.77–2.30	1.27–1.43
80–120	NO_2 twisting	2.25–2.48	1.48–1.68
140–450	Ring deformation	2.40–3.38	1.48–2.47
550–760	NO_2-ring deformation and NO_2 wagging	1.07–1.45	0.79–1.09
760–1,230	Ring stretching and N–N stretching	1.26–2.62	1.01–1.72
1,270–1,330	NO_2 symmetric stretching	1.21–1.56	1.12–1.39
1,330–1,460	CH_2 twisting, H_2 of CH_2 wagging, and HCH bending	1.62–2.18	1.52–2.14
1,480–1,490	NO_2 asymmetric stretching	1.29–1.49	1.63–1.66
2,900–3,000	CH_2 stretching	1.70–2.44	1.40–2.14

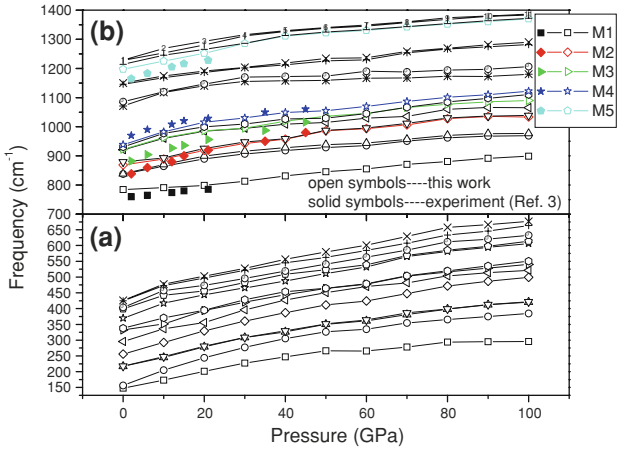

Fig. 6 Pressure-induced frequency shifts of **a** ring deformation modes and **b** ring stretching and N–N stretching modes for HMX

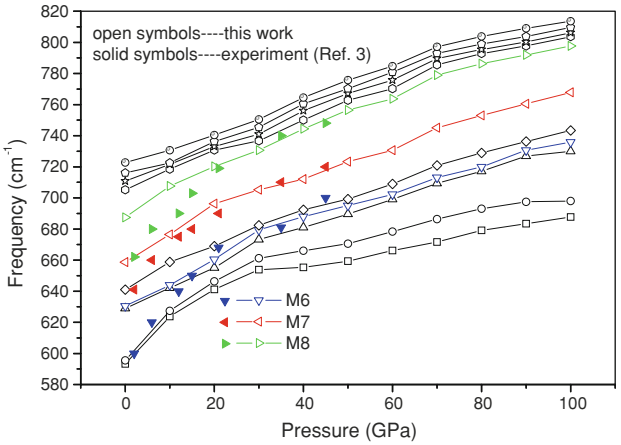

Fig. 7 Pressure-induced frequency shifts of NO_2-ring deformation and NO_2 wagging for HMX

2.12 cm^{-1}/GPa, respectively. This shows that the N–N bonds may be easily compressed in HMX. Another feature of the N–N stretching modes is that they mix strongly with the CH_2 rocking and twisting vibrations. The N–N stretching modes are related to the HMX decomposition reactions: N–N homolysis and HONO elimination [72]. Therefore, the strong mixing between the N–N stretching and the CH_2 rocking and twisting vibrations provides potential vibrational channels for the above decomposition.

Figure 7 shows the pressure-induced frequency shifts of NO_2-ring deformation and NO_2 wagging for HMX together with available experimental data. The calculated results reproduce the experimental trend of the frequency shifts of these modes. It is obvious that the agreement between the calculated and experimental results varies with compression. These modes shift toward higher vibrational frequencies with the increasing pressure. The NO_2-ring deformation modes are coupled to the N–N stretching vibrations. It is seen from Table 2 that these modes are quite insensitive to pressure. The frequency shifts of NO_2 stretching modes for HMX are displayed in Fig. 8. The

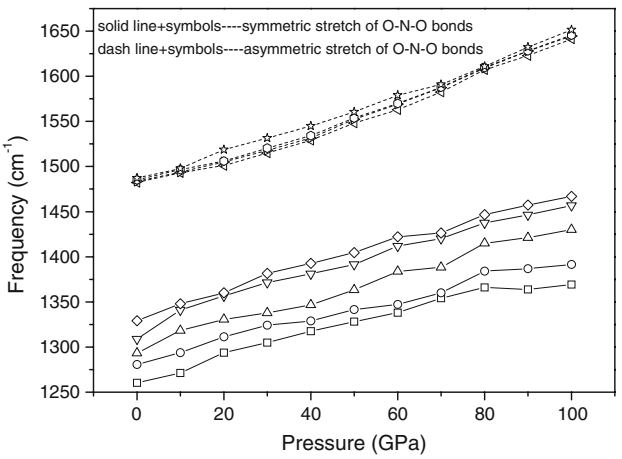

Fig. 8 Pressure-induced frequency shifts of NO_2 stretching modes for HMX

NO_2 stretching modes have frequencies higher than the N–N stretching vibrations. An important feature of the NO_2 stretching modes is that they are strongly coupled to the CH_2 stretching and twisting vibrations. This is because the

NO_2 and CH_2 locations on the periphery of the HMX molecules are very close. The mixing provides potential vibrational channels for the decomposition of HMX. In Table 2, it is interesting to note that under high pressure, the pressure-induced frequency shifts of NO_2 asymmetric stretching are larger than those of NO_2 symmetric stretching modes. Moreover, the NO_2 asymmetric stretching modes have larger frequency shifts under high pressure than under low pressure. This indicates that the NO_2 asymmetric stretching modes are quite sensitive to pressure, especially under high pressure. Therefore, it can be inferred that the vibrational modes of these side groups act as important vibrational channels for H migration reactions. These findings are supported by the experimental results [73] that the torsion motions of the NO_2 groups may act as doorway through which kinetic energy can flow into the molecule from its surroundings since the torsion motions of the molecule's functional groups are usually supposed to be highly coupled to the other moiety of the molecule.

Figure 9a shows the pressure-induced frequency shifts of CH_2 twisting, H_2 of CH_2 wagging, and HCH bending modes for HMX. The frequency shifts of these vibrational modes are relatively large under pressure. Moreover, these modes are strongly crossed. This large pressure dependence of the CH_2 vibrational modes is attributed to their locations on the HMX molecules. The frequency shifts of CH_2 stretching modes are displayed in Fig. 9b. The CH_2 stretching modes have frequencies higher than the CH_2 twisting, H_2 of CH_2 wagging, and HCH bending vibrations. As with the above CH_2 modes shown in Fig. 9a, the CH_2 stretching modes have large frequency shifts under compression. These modes are coupled strongly to the NO_2 stretching vibrations. This mixing provides important vibrational channels for the HMX decomposition reactions.

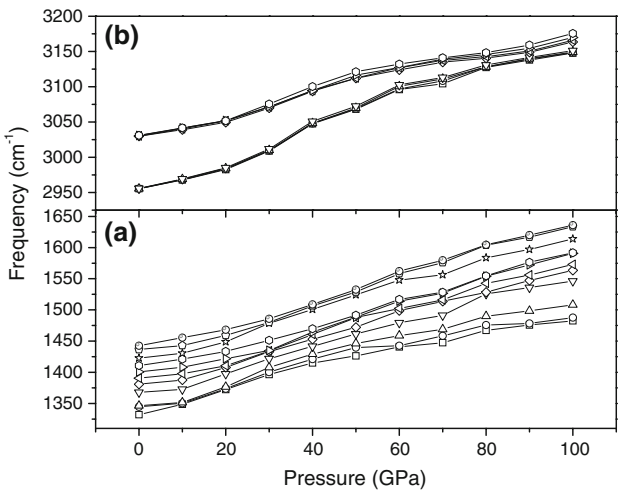

Fig. 9 Pressure-induced frequency shifts of **a** CH_2 twisting, H_2 of CH_2 wagging, and HCH bending modes and **b** CH_2 stretching modes for HMX

4 Conclusions

In this study, we have performed a systematic study of the structural, electronic, and vibrational properties of crystalline HMX under hydrostatic pressure of 0–100 GPa within density functional theory. The results show that as the pressure increases, both the structural parameter and the frequency shifts agree more closely with experimental results. The largest compression of the unit cell takes place in the pressure region of 0–30 GPa. The structure is much stiffer in the *a* and *c* direction than along the *b* axis, showing that the compressibility of HMX crystal is anisotropic. With the increasing pressure, the lattice constants and cell volumes calculated by LDA gradually approach these by GGA-PW91.

As the pressure increases, the band gap gradually decreases; moreover, the gap reduction is more pronounced in the low-pressure range compared to the high-pressure region. The band gaps calculated by LDA and GGA pseudopotential plane-wave method reproduce the trend of pressure-induced variation of band gap by all electron calculations. An understanding of the stabilities of HMX under compression based on the electronic structure shows that an applied pressure increases the impact sensitivity of HMX to detonation initiation.

The calculated pressure-induced frequency shifts indicate that the hydrostatic compression produces a more significant influence on the ring deformation and stretching vibrations than on other modes in the whole pressure range. The pressure also has a stronger effect on the vibrational modes associated with the motions of the CH_2 and NO_2 side groups, moreover, the NO_2 stretching modes are strongly coupled to the CH_2 vibrations. This shows that the vibrational modes of these side groups can act as important vibrational channels for H migration reactions. The mixing between different vibrational modes becomes stronger under compression. This strong mixing between the N–N stretching and the CH_2 rocking and twisting modes provides potential vibrational channels for a proposed concerted N–N homolysis and HONO elimination [68].

Acknowledgments This work was partly supported by the NSAF Foundation of National Natural Science Foundation of China and China Academy of Engineering Physics (10876013), the Research Fund for the Doctoral Program of Higher Education, and the Project-sponsored by the Scientific Research Foundation for the Returned Overseas Chinese Scholars, State Education Ministry.

References

1. Cooper PW, Kurowski SR (1996) Introduction to the technology of explosives. Wiley, New York
2. Akhaven J (1998) The chemistry of explosives. Royal Society of Chemistry, Cambridge, UK

3. Yoo C-S, Cynn H (1999) J Chem Phys 111:10229
4. Sorescu DC, Rice BM, Thompson DL (1999) J Phys Chem B 103:6783
5. Bedrov D, Smith GD, Sewell TD (2000) J Chem Phys 112:7203
6. Lewis JP, Sewell TD, Evans RB, Voth GA (2000) J Phys Chem B 104:1009
7. Brand HV, Rabie RL, Funk DJ, Diaz-Acosta I, Pulay P, Lippert TK (2002) J Phys Chem B 106:10594
8. Henson BF, Smilowitz L, Asay BW, Dickson PM (2002) J Chem Phys 117:3780
9. Smilowitz L, Henson BF, Asay BW, Dickson PM (2002) J Chem Phys 117:3789
10. Manaa MR, Fried LE, Melius CF, Elstner M, Frauenheim Th (2002) J Phys Chem A 106:9024
11. Lewis JP (2003) Chem Phys Lett 371:588
12. Hare DE, Forbes JW, Reisman DB, Dick JJ (2004) Appl Phys Lett 85:949
13. Stevens LL, Eckhardt CJ (2005) J Chem Phys 122:174701
14. Gump JC, Peiris SM (2005) J Appl Phys 97:053513
15. Hooks DE, Hayes DB, Hare DE, Reisman DB, Vandersall KS, Forbesa JW, Hall CA (2006) J Appl Phys 99:124901
16. Ye S, Koshi M (2006) J Phys Chem B 110:18515
17. Zerilli FJ, Kuklja MM (2006) J Phys Chem A 110:5173
18. Byrd EFC, Rice BM (2007) J Phys Chem C 111:2787
19. Zhu WH, Xiao JJ, Ji GF, Zhao F, Xiao HM (2007) J Phys Chem B 111:12715
20. Lian D, Lu L-Y, Wei D-Q, Zhang Q-M, Gong Z-Z, Guo Y-X (2008) Chin Phys Lett 25:899
21. Conroy MW, Oleynik II, Zybin SV, White CT (2008) J Appl Phys 104:053506
22. Dlott DD, Fayer MD (1990) J Chem Phys 92:3798
23. Tokmanoff A, Fayer MD, Dlott DD (1993) J Phys Chem 97:1901
24. Tarver CM (1997) J Phys Chem A 101:4845
25. Olinger BW, Roof B, Cady HH (1978) In: Symposium on high dynamic pressures. Commissariat al' Energie Atomique, Saclay, France, pp 3–8
26. Reisman DB, Forbes JW, Tarver CM, Garcia F, Hayes DB, Furnish MD, Dick JJ (2002) In: Proceedings of the 12th international detonation symposium. Office of Naval Research, Arlington, VA
27. Dick JJ, Hooks DE, Menikoff R, Martinez AR (2004) J Appl Phys 96:374
28. Baer MR, Hall CA, Gustavsen RL, Hooks DE, Sheffield SA (2007) J Appl Phys 101:034906
29. Reed EJ, Joannopoulos JD, Fried LE (2000) Phys Rev B 62:16500
30. Byrd EFC, Scuseria GE, Chabalowski CF (2004) J Phys Chem B 108:13100
31. Liu H, Zhao J, Wei D, Gong Z (2006) J Chem Phys 124:124501
32. Brand HV (2006) J Phys Chem B 110:10651
33. Xu X-J, Zhu W-H, Xiao H-M (2007) J Phys Chem B 111:2090
34. Zhu WH, Xiao HM (2007) J Solid State Chem 180:3521
35. Zerilli FJ, Hooper JP, Kuklja MM (2007) J Chem Phys 124:114701
36. Zerilli FJ, Kuklja MM (2007) J Phys Chem A 111:1721
37. Miao MS, Dreger ZA, Winey JM, Gupta YM (2008) J Phys Chem A 112:12228
38. Zhu WH, Zhang XW, Zhu W, Xiao HM (2008) Phys Chem Chem Phys 10:7318
39. Liu H, Zhao J (2008) Comput Mater Sci 42:698
40. Liu H, Zhao J, Du J, Gong Z, Ji G, Wei D (2007) Phys Lett A 367:383
41. Vanderbilt D (1990) Phys Rev B 41:7892
42. Payne MC, Teter MP, Allan DC, Arias TA, Joannopoulos JD (1992) Rev Mod Phys 64:1045
43. Kresse G, Furthmüller J (1996) Phys Rev B 54:11169
44. Fischer TH, Almlof J (1992) J Phys Chem 96:9768
45. Ceperley DM, Alder BJ (1980) Phys Rev Lett 45:566
46. Perdew JP, Zunger A (1981) Phys Rev B 23:5048
47. Choi CS, Boutin HP (1970) Acta Crystallogr Sect B 26:1235
48. Gonze X (1997) Phys Rev B 55:10337
49. Perdew JP, Chevary JA, Vosko SH, Jackson KA, Pederson MR, Singh DJ, Fiolhais C (1992) Phys Rev B 46:6671
50. Murnaghan FD (1951) In: Finite deformation of an elastic solid. Dover Publications, New York, p 73
51. Hummer K, Puschnig P, Ambrosch-Draxl C (2003) Phys Rev B 67:184105
52. Meyer R, Köhler J, Homburg A (2002) Explosives. Wiley-VCH Verlag GmbH, Weinheim
53. Kuklja MM, Kunz AB (1999) J Appl Phys 86:4428
54. Younk EH, Kunz AB (1997) Int J Quantum Chem 63:615
55. Delley B (1990) J Chem Phys 92:508
56. Delley B (2000) J Chem Phys 113:7756
57. Perdew JP, Wang Y (1992) Phys Rev B 45:13244
58. Gilman JJ (1995) Philos Mag B 71:1957
59. Xiao H-M, Li Y-F (1995) Sci China B 38:538
60. Xiao H-M, Li Y-F (1996) Banding and electronic structures of metal azides. Science Press, Beijing, p 88 (in Chinese)
61. Zhu WH, Xiao HM (2008) J Comput Chem 29:176
62. Zhu WH, Zhang XW, Wei T, Xiao HM (2008) Chin J Chem 26:2145
63. Zhu WH, Zhang XW, Wei T, Xiao HM (2009) J Mol Struct: Theochem 900:84
64. Gilman JJ (1979) J Appl Phys 50:4059
65. Gilman JJ (1998) Philos Mag Lett 77:79
66. Gilman JJ (1993) Philos Mag B 67:207
67. Gilman JJ (1994) Mech Mater 17:83
68. Kuklja MM, Stefanovich EV, Kunz AB (2000) J Chem Phys 112:3417
69. Luty T, Ordon P, Eckhardt CJ (2002) J Chem Phys 117:1775
70. Kuklja MM, Kunz AB (2000) J Appl Phys 87:2215
71. Botcher TR, Landouceur HD, Russel TR (1998) In: Schmidt SC, Dandekar DP, Forbes JW (eds) Shock compression of condensed matter—1997, Proceedings of the APS Topical Group. AIP, Woodbury, New York
72. Lewis JP, Glaesemann KR, VanOpdorp K, Voth GA (2000) J Phys Chem A 104:11384
73. Kirin D, Volovsek V (1997) J Chem Phys 106:9505